

## Effects of Hydrogen in Stress Triaxiality of API 5L X70 Steel

B. B. Freitas<sup>a</sup>, L. R. O. Costa<sup>a</sup>, T. A. A. dos Santos<sup>b</sup>, D. S. dos Santos<sup>a\*</sup> 

<sup>a</sup>Universidade Federal do Rio de Janeiro (UFRJ), Programa de Engenharia Metalúrgica e de Materiais (PEMM), Instituto Alberto Luiz Coimbra de Pós-Graduação e Pesquisa de Engenharia (COPPE), 21941-972, Rio de Janeiro, RJ, Brasil.

<sup>b</sup>Universidade Federal de Minas Gerais, 31270-901, Belo Horizonte, MG, Brasil.

Received: January 27, 2023; Revised: April 15, 2023; Accepted: May 11, 2023

Hydrogen embrittlement (HE) in API 5L X70 steel was investigated by testing notched and unnotched uniaxial tensile specimens and single-edge tension specimen, SE(T). Apparent hydrogen diffusivity ( $D_{app} = 1.4 \times 10^{-10} \text{ m}^2/\text{s}$ ) and solubility ( $S_{app} = 4.9 \text{ mol H/m}^3$ ) were determined by electrochemical hydrogen permeation tests. Through mathematical fitting, it was possible to separate the strong traps present at the beginning of the first permeation curve ( $\phi = 0.43 \text{ mol H/m}^3$ ). Uniaxial tensile tests showed a loss of ductility of up to 33% in the hydrogenated condition. Fracture mechanics tests exhibited a toughness decrease of 14% after exposure to hydrogen. The high resistance to HE was presented suggesting that these microalloyed steels can solubilize hydrogen in the matrix with low segregation, reducing the impact on embrittlement. A mix of ductile and quasi-cleavage fracture was observed in the hydrogenated samples with an increased stress triaxiality.

**Keywords:** API steel, Hydrogen embrittlement, Single-edge tension specimen, Notched tensile strength; Stress triaxiality.

### 1. Introduction

API 5L X70 steels are used in oil and natural gas transport pipelines and are therefore subjected to different environments and operating conditions that can affect their life cycle<sup>1</sup>. One of the main reasons for the degradation of the mechanical properties of these steels is the exposure to hydrogen (H) in service. High hydrogen concentrations in the pipeline can provoke some reduction on the mechanical properties of the steel, such as loss of ductility and mechanical strength<sup>2,3</sup>, causing hydrogen embrittlement, HE. The susceptibility of these steels to HE has been investigated by experimental tests<sup>4-8</sup> and computational simulations<sup>9-12</sup> by several authors over the years, but the critical H concentration in pipeline steels<sup>2</sup> is still not fully elucidated. This concentration is strongly dependent on different aspects of the steel being: microstructure, hardness, precipitates, and elements in solid solution.

Hydrogen diffusion behavior has been studied through electrochemical hydrogen permeation (EHP)<sup>4-8,13-20</sup> to understand physical variables such as solubility and diffusivity of H in steels. In the last decades, numerous authors have performed different mechanical tests with notched specimens in the presence of H<sup>9,10,21-25</sup> to address the critical conditions of hydrostatic stress and hydrogen concentration. In general, it has been observed that HE increases when the stress triaxiality conditions are higher<sup>25</sup>. The maximal triaxial stress state is responsible for a high volumetric strain that favors H accumulation, in addition to contributing to crack propagation<sup>9</sup>.

In this context, the objective of this study is to analyze the diffusivity and solubility of hydrogen based on theoretical and experimental calculations. The effects of H in API 5L X70 steel under different plastic constraints were also analyzed through uniaxial tensile tests and fracture mechanics tests in single edge notch tension specimens, SE(T), to characterize the behavior of hydrogen under triaxial stress in different geometries.

### 2. Experimental

#### 2.1. Materials and microstructure

API 5L X70 steel containing: 0.1C - 1.4Mn - 0.08(V, Nb, Ti), Fe balance in wt%, were used in this study. All tests were performed on mid layer specimens taken in a longitudinal direction. For the metallographic analysis, an optical microscope (OM), Olympus BX60M, and a scanning electron microscope (SEM) Tescan Vega3 and energy dispersive spectroscopy (EDS) in samples chemically etched with Nital 5% were used. Fracture surfaces were investigated using secondary electron images obtained with SEM, operating at 20kV.

#### 2.2. Electrochemical Hydrogen Permeation Test

EHP tests were performed using a double cell<sup>13-15</sup> at room temperature and with 1mm thick samples,  $L$  ( $x = [0, L]$ ). From these samples, experimental and theoretical curves were obtained. The experimental curve (continuous line), used for the apparent diffusivity ( $D_{app}$ ) calculations, considers the strong and the weak traps and diffusible hydrogen in the lattice. The sigmoidal fit curve corresponds to the evolution

\*e-mail: [dilson@metalmat.ufjf.br](mailto:dilson@metalmat.ufjf.br)

of the hydrogen flow ( $J_L$ ) as a function of time ( $t$ ). Assuming that the apparent hydrogen diffusivity ( $D_{app}$ ) does not vary with concentration, this relationship is given by Equation 1<sup>13</sup>:

$$J_L = J_\infty \left[ 1 - \frac{4}{\pi} \sum_{n=1}^{\infty} \frac{(-1)^n}{2n+1} \exp\left(\frac{-(2n+1)^2 \pi^2 D_{app} t}{4L^2}\right) \right] \quad (1)$$

The electrochemical cells were separated by the working electrode. In the first cell, a cathodic current was applied to generate hydrogen, using 0.1 M H<sub>2</sub>SO<sub>4</sub> + 2 mg/l As<sub>2</sub>O<sub>3</sub> solution. In the second cell, a slight anodic potential was applied to promote the oxidation of all hydrogen atoms diffusing through the sample. The second compartment, responsible for hydrogen detection, was filled with 0.1 M NaOH solution<sup>14,15</sup>.

A cathodic current equal to 80 A/m<sup>2</sup>, was applied in the hydrogen generation side, using the galvanostatic/potentiostatic method<sup>13-15</sup>. When a steady state was reached, the cathodic current was interrupted and the hydrogen flux decreased to values close to the background current ( $\sim 10^{-9}$  A). A second hydrogen permeation was performed using the same cathodic current to evaluate hydrogen permeation after filling the traps.

The apparent hydrogen diffusivity,  $D_{app}$ , was determined by break-through time,  $t_b$ , Equation 2 in the experimental curves<sup>13,14</sup>.

$$D_{app} = 0.76 \frac{L^2}{\pi^2 t_b} \quad (2)$$

The apparent solubility value ( $S_{app}$ ) was calculated by Equation 3:

$$S_{app} = S_{eff} + \varphi = \frac{J_\infty L}{D_{eff}} + \varphi \quad (3)$$

For the theoretical calculations of effective diffusivity ( $D_{eff}$ / Equation 2) and effective solubility ( $S_{eff}$ / Equation 3) a time correction was used, which disregards the strong traps that delay H permeation. The hydrogen concentration ( $\varphi$ ) necessary to fill the traps at the beginning of the permeation can be calculated from Faraday's law, assuming that the actual density has the same value as the steady-state hydrogen flux,  $J_\infty$ , as described in Equation 4<sup>14</sup>:

$$\varphi = \frac{\Delta t' i_0}{FAL} = \frac{\Delta t' J_\infty}{L} \quad (4)$$

Trap densities were obtained through ( $N_T$ ), Equation 5<sup>4,26</sup> was used, with  $N_a$  corresponding to the Avogadro constant and  $D_L$  to the diffusion coefficient in the lattice, free from traps:

$$N_T = \frac{N_a S_{app}}{3} \left( \frac{D_L}{D_{app}} - 1 \right) \quad (5)$$

### 2.3. Uniaxial tensile testing

Uniaxial tensile tests were performed in specimens with two different geometries using them as-received, stress-free

hydrogenated and hydrogenated applying elastic stress, at room temperature, under a strain rate of  $5 \cdot 10^{-4}$  s<sup>-1</sup>.

The unnotched cylindrical specimens followed the recommendations of ASTM E8/E8M standard<sup>27</sup>, with a diameter of 6 mm and a gage length of 35 mm. The cylindrical specimens, with V notch, followed the recommendations of the ESIS P6-98 (1998) standard<sup>28</sup>, with 6 mm internal diameter, 9 mm external diameter, 0.4 mm notch radius and gage length of 45 mm. The internal diameter of the specimens was used to calculate the stress. Details of the samples are shown in Figures 1a and 1b.

The specimens were hydrogenated for 24h in the same solution used in section 2.2 with a current density of 30, 80, 200 and 500 A/m<sup>2</sup>. In addition to the electrolytic load, an elastic stress of 280 MPa was applied to the notched and unnotched specimens, corresponding to 50% of the elastic stress of the tested unnotched specimens.

### 2.4. Finite element method

The finite element method (FEM) was used to investigate hydrogen concentration through simulation in notched specimens. The model used 2D axisymmetric approximation with linear quadrilateral approximation elements. Ansys® software was used for finite element calculation, with mesh refinement at the notch tip (Figure 1b). The model was held in the lower fixation region of the specimen and a load was applied to the upper fixation region. The initial and boundary conditions were the same as those used in the hydrogenation process, described in Section 2.3. Hydrostatic stress and plastic strain calculations were then performed<sup>9,29</sup>.

Equation 6 was used to calculate the hydrogen concentration profile<sup>9</sup>:

$$C_H = \phi C_0 \exp\left[\frac{V^* \sigma_h}{RT}\right] \cdot (1 + \alpha \varepsilon_p) \quad (6)$$

where  $C_H$  is the hydrogen concentration,  $\phi$  is the hydrogen activity,  $\alpha$  is the Ramberg Osgood coefficient,  $C_0$  is the reference concentration,  $V^*$  is the molar volume,  $\sigma_h$  is the hydrostatic stress,  $R$  is Boltzmann constant,  $T$  is the temperature in Kelvin,  $\alpha$  is a constant and  $\sigma_h$  and  $\varepsilon_p$  are the hydrostatic stress and the plastic strain, respectively.

### 2.5. Fracture mechanics

Fracture mechanics tests were performed in SE(T) specimens at room temperature, following the BSI standard<sup>30</sup>. The tests were carried out in as-received and stress-free hydrogenated samples under the same conditions as in Section 2.3 with a current density of 80 A/m<sup>2</sup>. The dimensions of the specimens are shown in Figure 1c and the value of  $a_0/W$  is 0.5. The dimensions were based on previous studies carried out in pipe steels<sup>31-36</sup> and tend to a plane state strain, which shows the triaxial stress effect<sup>37</sup>.

To estimate the maximum value of  $J^*$ , the elastic and plastic contributions to the strain energy of a notched specimen under mode I strain were considered<sup>38</sup>. Thus, Equation 7, based on the BSI standard<sup>30</sup>, was used for  $J^*$  calculations.

$$J^* = \frac{K^2}{E'} + \left( \frac{n_p U_p}{B(W - a_0)} \right) \quad (7)$$

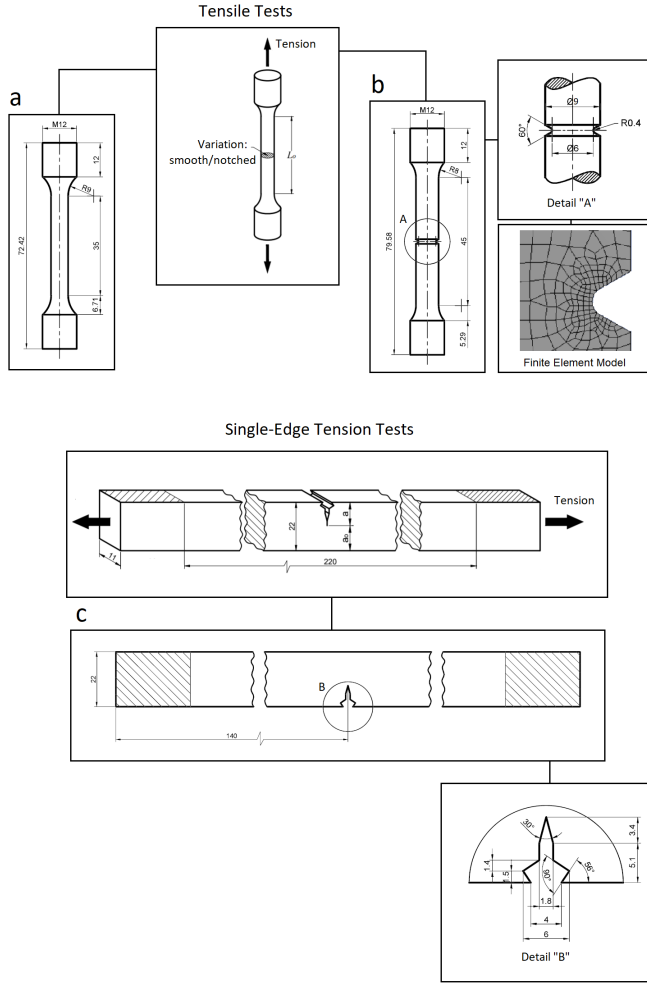


**Figure 1.** Specimens for: (a) stress-strain unnotched; (b) stress-strain notched; (c) single-edge tension specimen.

where  $K$  is the elastic stress intensity factor,  $E'$  the longitudinal elastic modulus in plane strain,  $n_p$  is a dimensionless geometry factor,  $U_p$  represents the plastic area under the curve during load displacement,  $B$  is the sample thickness,  $W$  the width and  $a_0$  is the initial crack length. To solve Equation 7, complementary functions were used<sup>30</sup>. However, due to limitation for specimens with a  $W/B = 2$ , the dimensionless factor of the “ $n_p$ ” geometry was calculated according to Equation 8<sup>38</sup>. This Equation is a 5th order polynomial fit, valid in the range of  $0.2 \leq a_0/W \leq 0.7$ , calculated for a ratio of  $H/W=10$  as follows.

$$n_p = 1.07 - 1.77 \frac{a_0}{W} + 7.81 \left(\frac{a_0}{W}\right)^2 - 18.30 \left(\frac{a_0}{W}\right)^3 + 15.29 \left(\frac{a_0}{W}\right)^4 - 3.08 \left(\frac{a_0}{W}\right)^5 \quad (8)$$

### 3. Results

#### 3.1. Microstructure

Figures 2a and 2b show the microstructure of API 5L X70 steel, where finely dispersed grains are observed in the

matrix. The microstructural analyses revealed the following components: polygonal ferrite (PF), acicular ferrite (AF), ferrite-bainite (FB) and upper bainite (UB). PF is an equiaxed microstructure, while AF is irregular, with well-defined contours. The FB phase has large grains with not clearly identified boundaries. UB appears in laths, formed from the limits of austenite<sup>39</sup>. In Figure 2b tiny particles, probably carbon rich, are distributed along the grain boundaries<sup>8</sup>. This microstructure agrees with what is expected for a high-strength micro-alloyed steel (HSLA)<sup>1,7,39-41</sup>.

#### 3.2. Electrochemical Hydrogen Permeation

Figure 3 shows the hydrogen permeation curves for the first (3.a) and second permeation (3.b). Figure 3.c shows a comparison between both permeations with the normalized steady flow.

It can be seen in Figures 3a and 3b, that the experimental curves are similar to the fitted curve (dash-dot) demonstrating convergence in the theoretical calculations. It can be supposed that a local equilibrium was quickly reached<sup>42</sup>, indicating agreement in the amount of inclusions found.

The initial hydrogen concentration ( $\phi$ ) was calculated<sup>14,16</sup> through the initial area between the two permeations (Figure 3c) with the integral defined between

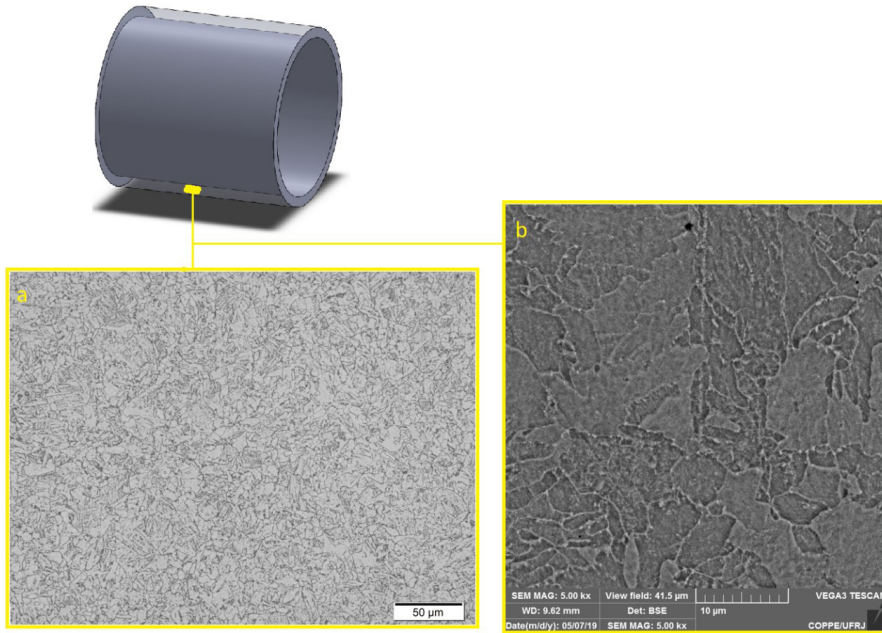


**Figure 2.** Microstructure of API 5L X70 steel: (a) OM and (b) SEM.

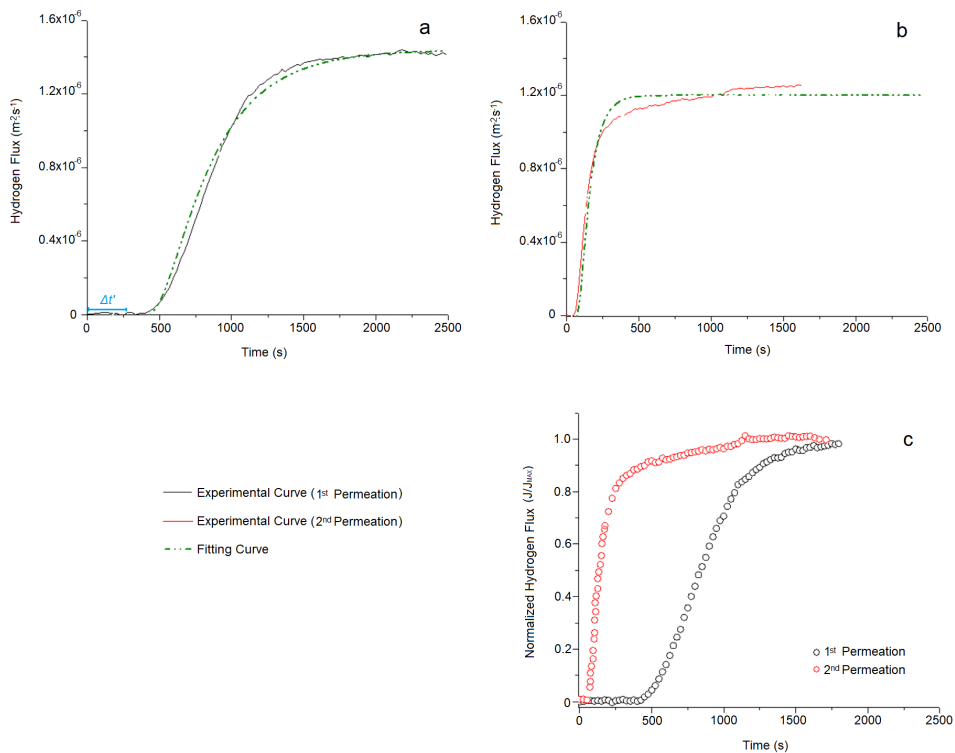


**Figure 3.** Electrochemical hydrogen permeation curves (API 5LX70): (a) first permeation, (b) second permeation, (c) comparison between first and second permeation.

zero and the time related to the filling of the strong traps. The calculated value was  $0.5 \text{ mol H/m}^3$ . This result was similar to the  $\phi$  calculated (Equation 4) and shown in Table 1.

Table 1 summarizes the experimental and calculated hydrogen diffusivity and solubility values for API 5L X70 steel,  $D_{app}$  and  $S_{app}$ ,  $D_{eff}$  and  $S_{eff}$ , respectively.  $D_{eff}$  is greater than  $D_{app}$  due to the subtraction of the initial delay

from the experimental permeation curve<sup>14</sup>. The apparent and effective solubility results of the first permeation differ due to the presence of deep traps at the beginning of the curve. Strong traps tend to be filled in the experimental curve of the first permeation<sup>1,7,14,18</sup>. These traps capture H, resulting in  $S_{app}$  being higher than  $S_{eff}$ . However, when analyzing the solubilities ( $S_{app}$  and  $S_{eff}$ ) of the second permeation, it was

observed that a local equilibrium was reached<sup>42</sup>, which caused the solubility values to converge, due to the approximation of the Fickian behavior.

The lattice diffusivity value<sup>1,20,43,44</sup>, was used to calculate the lattice solubility,  $S_L=0.2 \text{ mol H/m}^3$ . Thus, 96% of  $S_{app}$  is attributed to the strong and weak traps of the API steel. Both papers<sup>19,20</sup> showed that solubility of hydrogen is strongly influenced by strong and weak traps and that the lattice solubility hydrogen is between 2.4 – 4%, showing good convergence with the values in Table 1.

Trap density calculation ( $N_T$ ) was performed using Equation 5<sup>26</sup>, other equations can be found in the literature<sup>42,45-48</sup>.  $N_T$  value of the first permeation corresponds to the strong, weak and lattice trap densities. The second permeation has the lowest  $N_T$  value due to the strong trap saturation of the first permeation<sup>4,46,49-51</sup>. Comparing the results of trap density between the first and second permeation, a decrease of two orders of magnitude is observed. Thus, it can be concluded that the strong trap densities are of the order of  $10^{25}$ . API 5L X70 steels have a high defect density, as well as dislocations, vacancies, grain boundaries, and some carbides<sup>49</sup>. The initial trap density related to the presence of dislocations is cited in the literature as being in the order of  $10^{13} \text{ m}^{-2}$  and  $10^{14} \text{ m}^{-2}$  in acicular ferrite<sup>51-53</sup>. In addition to dislocations, in some studies  $N_T$  correlates with grain boundaries and triple junctions<sup>4</sup>, vacancies, and carbides<sup>49</sup>.

### 3.3. Uniaxial tensile test

Figure 4a shows the stress x strain curves for the following samples: as-received unnotched (UAR), hydrogenated applying elastic tension unnotched (UHT50%), as-received notched (NAR), hydrogenated applying elastic tension notched (NHT50%) and hydrogenated applying no elastic tension notched with current density: 30 A/m<sup>2</sup> (NHT0\_I\_030), 80 A/m<sup>2</sup> (NHT0\_I\_080), 200 A/m<sup>2</sup> (NHT0\_I\_200) and 500 A/m<sup>2</sup> (NHT0\_I\_500). Figure 4b presents a comparison of the ductility loss values found by other authors<sup>9</sup> and this

study for different API 5L steel grades according to the applied current density.

Figure 4a shows that hydrogen caused a small reduction in ductility in unnotched and notched samples. There was also an enhanced loss of mechanical strength in NHT0\_I\_500, compared to the other samples. Hydrogen segregation at the tip of the notch, the highest stress concentration region, contributed to a greater mechanical strength decrease. The effect of hydrogen concentration at the tip of the notch was proven through a simulation, shown in Figure 5e. These results indicate that HE is controlled by stress and critical local hydrogen concentration which only occurs when the combination of both factors is satisfied in a specific microstructure<sup>54</sup>.

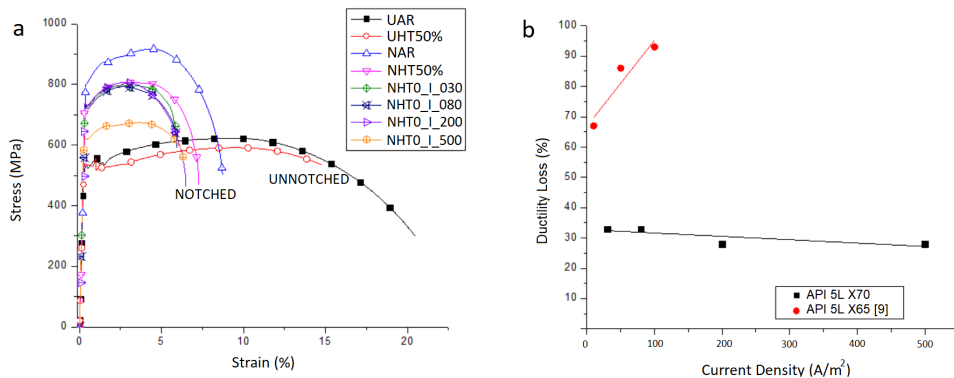
An increase in yield strength is observed in all hydrogenated samples, followed by a decrease in stress until a plateau is formed between the elastic and plastic regions (Figure 4a)<sup>22,55</sup>. Such evidence of hydrogen interaction with plasticity suggests that hydrogen may interfere with the propagation of the slip band at the beginning of the tensile test. For the notched samples, the yield strength is higher than unnotched specimens, due to the stress concentration factor (Kt). The Kt calculated for notched samples were 2.5<sup>54,56-57</sup>.

Figure 4.b shows that there was no loss of ductility of API 5LX70 steel for all tested current densities. When compared to notched samples of an API 5L X65 steel<sup>9</sup>, the loss of ductility becomes evident even for current densities of 50 and 100 A/m<sup>2</sup>. The literature shows strong evidence that a refined grain microstructure containing acicular ferrite is responsible for a high resistance to HE<sup>8,58</sup>, this microstructure is presented in API 5L X70 steel.

The average of the uniaxial tensile test results is shown in Table 2. For unnotched specimens, the ductility of the pair of samples is within the values accepted by the API 5L 2000 standard<sup>32</sup>. For notched samples, the presence of hydrogen decreased the ductility by up to 33%. Moreover, it is observed that all hydrogenated notched samples showed

**Table 1.** Electrochemical hydrogen permeation results.

Permeation	$D_{app} \cdot 10^{-10}$ (m <sup>2</sup> /s)	$S_{app}$ (mol H/m <sup>3</sup> )	$\Delta t'$ (s)	$D_{eff} \cdot 10^{-10}$ (m <sup>2</sup> /s)	$S_{eff}$ (mol H/m <sup>3</sup> )	$S_L$ (mol H/m <sup>3</sup> )	$\phi$ (mol H/m <sup>3</sup> )	$N_T$ (m <sup>-3</sup> )
<b>First</b>	1.4	4.9	283	3	4.5	0.2	0.4	$2.6 \times 10^{25}$
<b>Second</b>	11.3	0.6	28	21.3	0.6	0.2	0	$3.5 \times 10^{23}$



**Figure 4.** (a) Stress x Strain diagram in as-received and hydrogenated samples; (b) Comparison of ductility loss for API 5L steels.

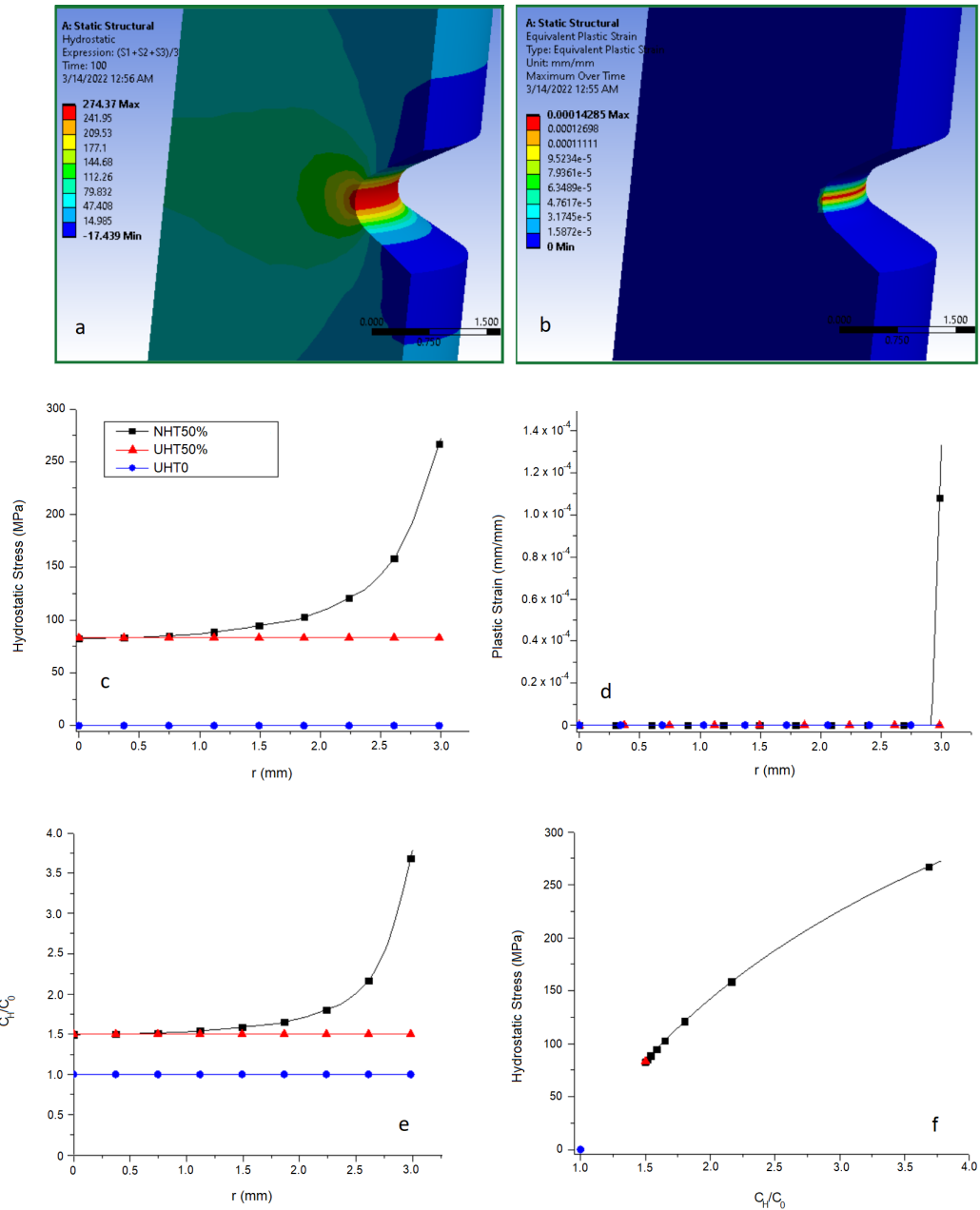


**Figure 5.** FEM of hydrogenated tensile samples with and without tension (a) finite element simulation with of hydrostatic stress; (b) finite element simulation of plastic strain; (c) hydrostatic stress profile along the radius; (d) plastic strain profile along the radius; (e) hydrogen concentration profile along the radius; (f) hydrostatic stress profile versus hydrogen concentration.

**Table 2.** Tensile test results for notched and unnotched specimens.

Condition	Yield Strength (MPa)	Ultimate Strength (MPa)	Total Deformation (%)	Ductility Loss (%)
UAR	538	618	20	-
UHT50%	544	600	16	20
NAR	793	911	9	-
NHT50%	742	810	7	22
NHT0_I_030	726	794	6	33
NHT0_I_080	732	790	6	33
NHT0_I_200	735	807	6,5	28
NHT0_I_500	625	673	6,5	28

a slight reduction in maximum stress, compared to UAR. In this study, it is demonstrated that the presence of notches intensifies the embrittlement<sup>9,55</sup> due to the combined effects of hydrogen with the plastic restriction caused by the notch.

Thought, several uniaxial tensile tests and hydrogen permeability tests can be found in the literature to evaluate pipeline steels<sup>6,9,22</sup>, implying high resistance to HE in API steels, in agreement with this study.

### 3.4. Finite element analysis

Figure 5 represents the finite element analysis, FEA, to evaluate the hydrostatic stresses (Figure 5a) and plastic strain (Figure 5b) at local scale in the notch of the NHT50% sample. Figures 5c and 5d diagrams show hydrostatic stress and plastic strain of the NHT50%, UHT50% and UHT0 samples, comparing notched and unnotched specimen. The center of the specimen is  $r = 0$  and the periphery  $r = 3$  mm. Figures 5e and 5f present the normalized hydrogen concentration ( $C_H/C_0$ ) across the radius of the sample and the relationship with the hydrostatic stress.

In Figures 5a and 5b, greater hydrostatic stress and plastic strain are observed at the tip of the notch, indicating higher susceptibility to HE in this region. Figures 6c and 6d show that the maximum hydrostatic stress and plastic strain occur at the tip of the notch<sup>9</sup>, NHT50% sample. In the samples without a notch, the hydrostatic stress remains constant depending on the elastic stress applied in the hydrogenation. The plastic strain was practically zero at the tip of the notch in the NHT50% sample. This condition proved to be sufficient to maintain the ductility of the steel at a macroscopic level (see Figure 4a).

Figures 5e and 5f present the results of hydrogen concentration profiles normalized by the maximum concentration<sup>9,59</sup>. Applying 50% of the elastic tension during hydrogenation increased the hydrogen concentration in 73% (NHT50%) and 33% (UHT50%), Figure 5e. Although the

total plastic strain is very small for the notched samples, there is a significant concentration of hydrogen at the tip of the notch due to hydrostatic stress exponential growth, as shown in Figure 5f.

### 3.5. Fracture mechanics

The toughness of API 5L X70 steel was characterized considering the elastoplastic regime. Figures 6a and 6b show the load versus crack mouth opening displacement (CMOD) and the maximum load versus the normalized area based on the literature<sup>31,33</sup>.

Figure 6a shows that the CMOD at maximum stress is lower for the hydrogenated pre charging (HPC) sample, indicating a decrease in toughness in this SE(T) specimen. The hydrogen has facilitated the dislocation movements that were previously stuck, decreasing the local energy, with a reduction in the maximum load being observed.

Figure 6b presents a linear behavior between the maximum load and the normalized area of SE(T) specimens without hydrogen charging (WHC). Dividing the ordinate axis by its abscissa, a constant value ( $\rho$ ) can be obtained, indicated in Table 3. In the literature<sup>31,33</sup>, specimens with different dimensions were tested, whose  $\rho$  values show convergence with the one obtained in this study.

The  $K_t$  calculated for SE(T) geometry was obtained by the following Equation<sup>60</sup>:

$$K_t = \sigma \sqrt{\pi a} Y(r); \text{ where: } Y(r) = 1,12 - 0,231r + 10,55r^2 - 21,71r^3 + 30,382r^4.$$

The value was equal to 16.6, while the value of  $K_t$  for the tensile test on notched samples was 2.5. With these values, it is observed that even for high stress triaxiality, the hydrogenated steel presented good mechanical behavior.

Table 3 shows the fracture toughness values calculated at the maximum point of the curve. A reduction of the maximum load is noted for the HPC samples compared to those without hydrogen charging, which is in agreement

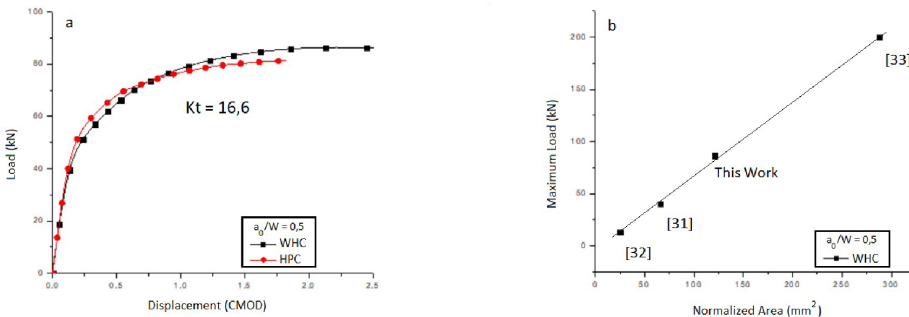


**Figure 6.** (a) P versus CMOD diagram, of as-received and hydrogenated SE(T) specimens with a  $a_0/W = 0.5$  ratio; (b) maximum values and normalized area taken from the literature and obtained in this work in SE(T) samples WHC.

**Table 3.** Fracture mechanics test results with hydrogen pre charging (HPC) and without hydrogen charging (WHC).

Condition	$P$ (kN)	$CMOD$ (mm)	$U_p$	$J_{el}^*$ (N/mm)	$J_{pl}^*$ (N/mm)	$n_p$	$J_{MAX}^*$ (N/mm)	Tenacity Loss (%)	$\rho$	$\Delta a$
WHC	86.5	2.1	155	94	916	0.7	1010	-	0.6	1.1
HPC	81.6	2	133	84	785	0.7	869	14	-	0.7

with previous works<sup>61</sup>. The result of  $J_{MAX}$  in WHC samples is similar to those presented in the  $J^*$ -resistance curves of some studies<sup>34,62</sup> with crack extension  $\Delta a=1.1$  mm. The CMOD and plastic area values calculated for the HPC sample show a slight decrease. Thereby, compared to WHC sample, a loss of fracture toughness of 14% can be observed in the presence of hydrogen (HPC sample). Different fracture toughness tests (by SE(T), SEN(B) and C(T) tests) are used depending on the level of conservatism that each one is proposed according to necessary requirements. However, this is not the only factor that exerts control over toughness results. The microstructure, the hardness and the amount of hydrogen introduced into the material are the most important points that can cause strong variation in the results of hydrogen embrittlement<sup>22,61-64</sup>. Hydrogen tends to accumulate in the regions of greater strain<sup>11,12,65</sup> and the dislocation mobility can be enhanced by the higher hydrogen concentration at the tip of the notch. However, the high resistance to HE suggests that these microalloyed steels can solubilize hydrogen in the matrix with low segregation, reducing the impact on embrittlement.

The  $n_p$  value (Table 3) complemented this study due to the geometric limitation of BSI Standard<sup>30</sup>. Numerous

polynomial equations<sup>66-71</sup> also suggest adjustments to satisfy the  $a/W$  and  $W/B$ .

### 3.6. Fractographies

Figure 7 shows the fractographies of the mechanical tests. Figure 7a, UHT50% sample, shows the existence of dimples, which is a characteristic of ductile materials. The presence of hydrogen is indicated by regions morphologically so-called “fisheye”. The stress around the inclusions increases, promoting crack nucleation sites. It is implied that the weakening in this interface is a combination of three factors: the matrix/inclusion interface, the generated microcavities, and the stress field coming from the matrix around the inclusion. Figure 7b, NHT50% specimen, shows a fractography with a predominant quasi-cleavage micromechanism with fisheye presence. Such results indicate that this fracture mode may be related to higher hydrogen concentration associated with hydrostatic stress (see Figure 5f)<sup>9,70</sup>.

Figure 7c shows the fractography of the SE(T) fracture mechanical test, HCP sample, region between pre-crack and crack growth. In Figures 7d and 7e, quasi-cleavage and micro-voids are visualized in the crack growth region.

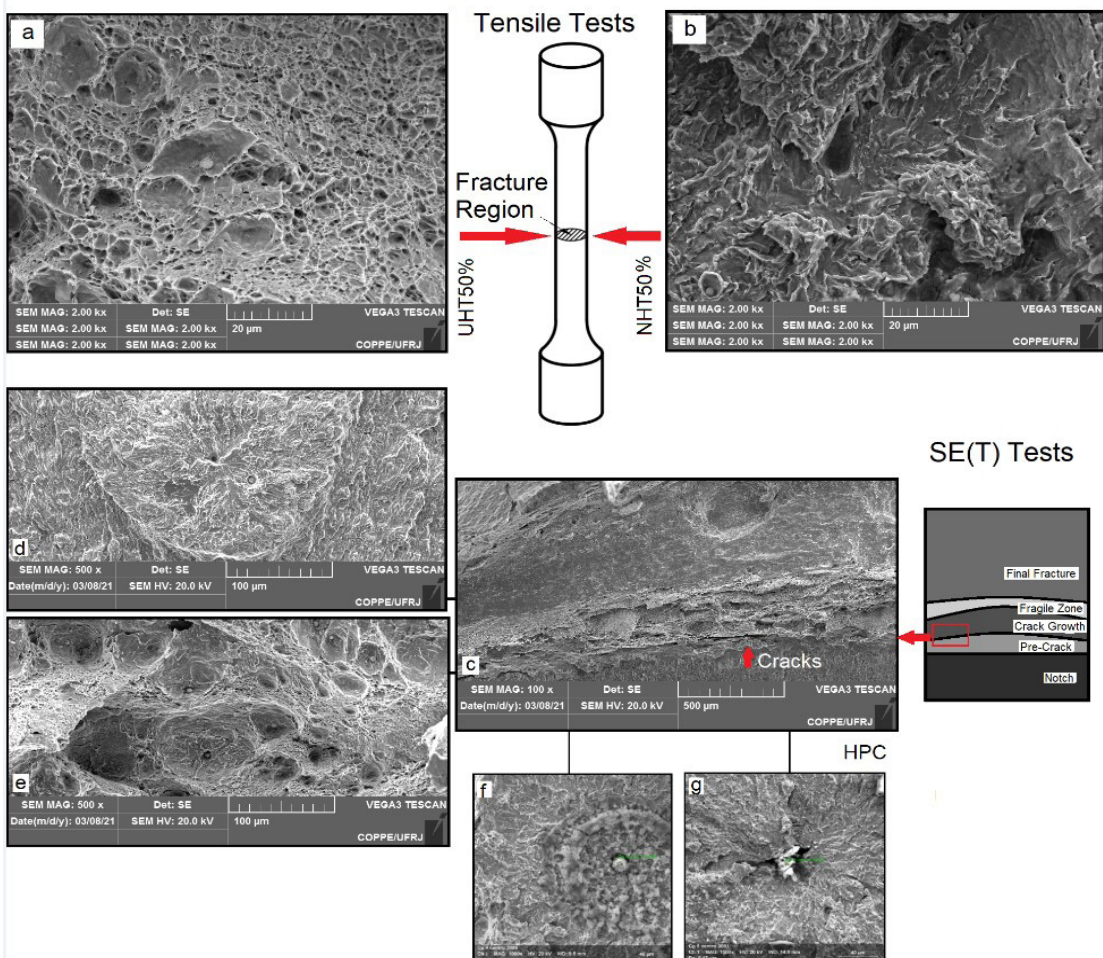


**Figure 7.** Fractographies of mechanical tests: (a,b) uniaxial tensile test, UHT50% and NHT50% samples; (c,d,e,f,g) fracture mechanic test, HCP sample.

Throughout the entire specimen, inclusions were found with trapped hydrogen, which could be identified through the fisheye morphology (Figures 7f and 7g). The inclusions and oxides found are dispersed in small amounts. It is noteworthy, however, that most of the inclusions in the center of the fisheye present aluminum in their composition, which proves the weak interaction of hydrogen with these types of inclusions. This distribution of defects in the microstructure shows points of higher local concentration of hydrogen<sup>72</sup>, favoring HE. Secondary cracks, parallel to the main fracture crack were also observed in the present study (Figure 7c).

#### 4. Conclusion

Hydrogen diffusivity, solubility, and also susceptibility to hydrogen embrittlement in API 5L X70 steel were investigated.

The hydrogen permeation tests were evaluated by apparent values and compared with theoretical fitting calculations. The fit calculations managed to separate the strong traps at the beginning of the curve ( $\phi = 0.43 \text{ mol H/m}^3$ ) and showed good agreement with the experimental curve. The experimental values of the first H permeation showed diffusivity equal to  $1.4 \times 10^{-10} \text{ m}^2/\text{s}$  and solubility of  $4.9 \text{ mol H/m}^3$ .

The uniaxial tensile test of notched and unnotched specimens showed that hydrogen promoted a minor loss of ductility, and the mechanical resistance for all tested current densities. Hydrogen was responsible for a 14% reduction in fracture toughness, indicating a high resistance to hydrogen embrittlement for varying conditions of stress triaxiality.

#### 5. Acknowledgments

The authors acknowledge the financial support from CAPES, CNPq, FAPERJ.

#### 6. References

- Haq AJ, Muzaka K, Dunne DP, Calka A, Pereloma EV. Effect of microstructure and composition on hydrogen permeation in X70 pipeline steels. *Int J Hydrogen Energy*. 2013;38(5):2544-56.
- Wang R. Effects of hydrogen on the fracture toughness of a X70 pipeline steel. *Corros Sci*. 2009;51(12):2803-10.
- Zafra A, Peral LB, Belzunce J. Hydrogen diffusion and trapping in A 42CrMo4 quenched and tempered steel: influence of tempering temperature. *Int J Hydrogen Energy*. 2020;45(55):31225-42.
- Thomas A, Szpunar JA. Hydrogen diffusion and trapping in X70 pipeline steel. *Int J Hydrogen Energy*. 2019;45(3):2390-404.
- Diaz A, Cuesta II, Martínez-Pañeda E, Alegre JM. Analysis of hydrogen permeation tests considering two different modelling approaches for grain boundary trapping in iron. *Int J Fract*. 2020;223:17-35.
- Sun D, Wu M, Xie F, Gong K. Hydrogen permeation behavior of X70 pipeline steel simultaneously affected by tensile stress and sulfate-reducing bacteria. *Int J Hydrogen Energy*. 2019;44(43):24065-74.
- Mohtadi-Bonab MA, Szpunar JA, Razavi-Tousi SS. A comparative study of hydrogen induced cracking behavior in API 5L X60 and X70 pipeline steels. *Eng Fail Anal*. 2013;33:163-75.
- Dong CF, Li XG, Liu ZY, Zhang YR. Hydrogen-induced cracking and healing behaviour of X70 steel. *J Alloys Compd*. 2009;484(1-2):966-72.
- Cayón A, Gutiérrez-Solana F, Arroyo B, Álvarez JA. Hydrogen embrittlement processes in microalloyed steel notched tensile samples. *Theor Appl Fract Mech*. 2021;112:102878-95.
- Toribio J, González B, Matos JC. Hydrogen embrittlement and notch tensile strength of pearlitic steel: a numerical approach. *Procedia Struct Integr*. 2020;28:2444-9.
- Olden V, Thaulow C, Johnsen R, Østby E, Berstad T. Influence of hydrogen from cathodic protection on the fracture susceptibility of 25%Cr duplex stainless steel - Constant load SENT testing and FE-modelling using hydrogen influenced cohesive zone elements. *Eng Fract Mech*. 2009;76(7):827-44.
- Sofronis P, Mcmeekinc RM. Numerical analysis of hydrogen transport near a blunting crack tip. *J Mech Phys Solids*. 1989;37(3):317-50.
- Boes N, Zochner H. Electrochemical methods for studying diffusion, permeation and solubility of hydrogen in metals. *J Less Common Met*. 1976;49:223-40.
- Cardenas AL, Silva RO, Eckstein CB, Santos DS. Hydrogen effect on 2.25Cr-1Mo-0.25V bainitic steel under aging heat treatment. *Int J Hydrogen Energy*. 2018;43(33):16400-10.
- Santos DS, Miranda PEV. Hydrogen diffusivity and solubility in crystalline and amorphous alloys. *J Mater Sci*. 1997;32:6311-5.
- Garcia DCS, Carvalho RN, Lins VFC, Rezende DM, Santos DS. Influence of microstructure in the hydrogen permeation in martensitic-ferritic stainless steel. *Int J Hydrogen Energy*. 2015;40(47):17102-9.
- Kim WK, Koh SU, Yang BY, Kim KY. Effect of environmental and metallurgical factors on hydrogen induced cracking of HSLA steels. *Corros Sci*. 2008;50(12):3336-42.
- Fallahmohammadi E, Bolzoni F, Fumagalli G, Re G, Benassi G, Lazzari L. Hydrogen diffusion into three metallurgical microstructures of a C-Mn X65 and low alloy F22 sour service steel pipelines. *Int J Hydrogen Energy*. 2014;39(25):13300-13.
- Zakroczymski T. Adaptation of the electrochemical permeation technique for studying entry, transport and trapping of hydrogen in metals. *Electrochim Acta*. 2006;51(11):2261-6.
- Frappart S, Feaugas X, Creus J, Thebault F, Delattre L, Marchebois H. Study of the hydrogen diffusion and segregation into Fe-C-Mo martensitic HSLA steel using electrochemical permeation test. *J Phys Chem Solids*. 2010;71(10):1467-79.
- Tao P, Ye F, Liu H, Gong J, Yang X, Barrett RA, et al. Dual-phase cohesive zone modelling and experimental validation for hydrogen-assisted cracking of 2205 duplex stainless steel. *Int J Press Vessels Piping*. 2021;190:104296-309.
- Asadipoor M, Pourkamali Anaraki A, Kadkhodapour J, Sharifi SMH, Barnoush A. Macro- and microscale investigations of hydrogen embrittlement in X70 pipeline steel by in-situ and ex-situ hydrogen charging tensile tests and in-situ electrochemical micro-cantilever bending test. *Mater Sci Eng A*. 2020;772:138762-73.
- Zhang S, An T, Zheng S, Li J, Li S, Chen L. The effects of double notches on the mechanical properties of a high-strength pipeline steel under hydrogen atmosphere. *Int J Hydrogen Energy*. 2020;45(43):23134-41.
- Najam H, Koyama M, Bal B, Akiyama E, Tsuzaki K. Strain rate and hydrogen effects on crack growth from a notch in a Fe-high-Mn steel containing 1.1 wt% solute carbon. *Int J Hydrogen Energy*. 2020;45:1125-39.
- Álvarez G, Zafra A, Belzunce FJ, Rodríguez C. Hydrogen embrittlement analysis in a CrMoV steel by means of sent specimens. *Theor Appl Fract Mech*. 2020;106:102450-7.
- Araújo DF, Vilar EO, Palma Carrasco J. A critical review of mathematical models used to determine the density of hydrogen trapping sites in steels and alloys. *Int J Hydrogen Energy*. 2014;39(23):12194-200.
- ASTM: American Society for Testing and Materials. ASTM E8/E8M: standard test methods for tension testing of metallic materials. West Conshohocken: ASTM International; 2016.
- ESIS: European Structural Integrity Society. ESIS P6-98: procedure to measure and calculate material parameters for the local approach to fracture using notched tensile specimens. Germany: ESIS; 1998.

29. Lesne L, Garat X, Schwinn V, Zmudzinsky Z, Alvarrez JA, Gutiérrez-Solana F, et al. Application of new fracture mechanics concepts to hydrogen damage evolution. Belgium: European Union; 2003.
30. BSI: British Standards Institution. BSI 8571: Standards Publication Method of test for determination of fracture toughness in metallic materials using single edge notched tension (SENT) specimens. United Kingdom: BSI; 2018.
31. Pussegoda LN, Tiku S, Park DY, Tyson WR, Gianetto J. J-Resistance results from multi-specimen and single-specimen surface notched SEN(T) geometry. In: 9th International Pipeline Conferences; 2012 Sep 24-28; Calgary, Alberta, Canada. Proceedings. New York: American Society of Mechanical Engineers; 2012. vol. 45141; p. 539-44.
32. Aguirre Torrico IF. Tenacidade à fratura em condições elasto-plásticas com corpos de prova não normalizados para aços API 5L: análise numérica e experimental [thesis]. Campinas: Universidade Estadual de Campinas; 2006.
33. Kofiani K, Nonn A, Wierzbiński T. New calibration method for high and low triaxiality and validation on SENT specimens of API X70. *Int J Press Vessels Piping*. 2013;111-112:187-201.
34. Francisco JCS, Moreno JRS, Bose WW Fo, Ruchert COFT. Effect of pre-crack in the fracture properties of steel pipes used in oil type API 5L X70. *J Braz Soc Mech Sci Eng*. 2016;38:2117-27.
35. Wang E, Zhou W, Shen G, Duan D. An experimental study on J(CTOD)-R curves of single edge tension specimens for X80 steel. In: 9th International Pipeline Conferences; 2012 Sep 24-28; Calgary, Alberta, Canada. Proceedings. New York: American Society of Mechanical Engineers; 2012. vol. 4, p. 241-8.
36. Weeks TS, Read DT. Comparison of J-integral from single specimen SE(T) tests on API-5L X100 line pipe steel. In: 25th International Offshore (Ocean) and Polar Engineering Conference; 2015 Jun 21-26; Waikoloa, HI. Proceedings. Cupertino, United States: International Society of Offshore and Polar Engineers; 2015.
37. Faleskog J, Gao X, Shih F. Cell model for nonlinear fracture analysis - I. Micromechanics calibration. *Int J Fract*. 1998;89:355-73.
38. Mathias LLS, Sarzosa DFB, Ruggieri C. Effects of specimen geometry and loading mode on crack growth resistance curves of a high-strength pipeline girth weld. *Int J Press Vessels Piping*. 2013;111-112:106-19.
39. Shin SY, Woo KJ, Hwang B, Kim S, Lee S. Fracture-toughness analysis in transition-temperature region of three American petroleum institute X70 and X80 pipeline steels. *Metall Mater Trans, A Phys Metall Mater Sci*. 2009;40:867-78.
40. Liu ZY, Li XG, Du CW, Lu L, Zhang YR, Cheng YF. Effect of inclusions on initiation of stress corrosion cracks in X70 pipeline steel in an acidic soil environment. *Corros Sci*. 2009;51(4):895-900.
41. Atkinson HV, Shi G. Characterization of inclusions in clean steels: a review including the statistics of extremes methods. *Prog Mater Sci*. 2003;48(5):457-520.
42. Oriani RA. The diffusion and trapping of hydrogen in steel. *Acta Metall*. 1970;18(1):147-57.
43. Turnbull A, Carroll MW. The effect of temperature and H<sub>2</sub>S concentration on hydrogen diffusion and trapping in a 13% chromium martensitic stainless steel in acidified NaCl. *Corros Sci*. 1990;30(6-7):667-79.
44. Kiuchi K, McLellan RB. The solubility and diffusivity of hydrogen in well-annealed and deformed iron. *Acta Metall*. 1983;31(7):961-84.
45. Oriani RA. The physical and metallurgical aspects of hydrogen in metals. In: 4th International Conference on Cold Fusion; Palo Alto, CA. Proceedings. Palo Alto: Electric Power Research Institute; 1993.
46. Krom AHM, Bakker AD. Hydrogen trapping models in steel. *Metall Mater Trans, B, Process Metall Mater Proc Sci*. 2000;31:1475-82.
47. McLellan R. Thermodynamics and diffusion behavior of interstitial solute atoms in non-perfect solvent crystals. *Acta Metall*. 1979;27(10):1655-63.
48. McNabb A. A new analysis of the diffusion of hydrogen in iron and ferritic steels. *Trans Metall Soc AIME*. 1963;227:618-45.
49. Ha HM, Ai JH, Scully JR. Effects of prior cold work on hydrogen trapping and diffusion in API X-70 line pipe steel during electrochemical charging. *Corrosion*. 2014;70(2):166-84.
50. Kumnick AJ, Johnson HH. Deep trapping states for hydrogen in deformed iron. *Acta Metall*. 1980;28(1):33-9.
51. Yang JR, Bhadeshia HKDH. The dislocation density of acicular ferrite in steel welds. *Weld J Res Suppl*. 1990;69:305-7.
52. Lehtinen A, Laurson L, Granberg F, Nordlund K, Alava MJ. Effects of precipitates and dislocation loops on the yield stress of irradiated iron. *Sci Rep*. 2018;8(1):1-11.
53. Sedighiani K, Traka K, Roters F, Raabe D, Sietsma J, Diehl M. Determination and analysis of the constitutive parameters of temperature-dependent dislocation-density-based crystal plasticity models. *Mech Mater*. 2021;164:104117-32.
54. Zafra A, Peral LB, Belzunze J, Rodríguez C. Effect of hydrogen on the tensile properties of 42CrMo4 steel quenched and tempered at different temperatures. *Int J Hydrogen Energy*. 2018;43(18):9068-82.
55. Lesage J, Chicot D, Bartier O, Zampronio MA, Miranda PEV. Influence of hydrogen contamination on the tensile behavior of a plasma ion nitrided steel. *Mater Sci Eng*. 2000;282(1-2):203-12.
56. Neuber H, Raven FA, Brock JS. Theory of notch stresses: principles for exact stress calculation. Berlin: Julius Springer; 1937.
57. Guedes D, Malheiros LC, Oudriss A, Cohendoz S, Bouhattat J, Creus J, et al. The role of plasticity and hydrogen flux in the fracture of a tempered martensitic steel: a new design of mechanical test until fracture to separate the influence of mobile from deeply trapped hydrogen. *Acta Mater*. 2020;186:133-48.
58. Park GT, Koh SU, Jung HG, Kim KY. Effect of microstructure on the hydrogen trapping efficiency and hydrogen induced cracking of linepipe steel. *Corros Sci*. 2008;50(7):1865-71.
59. Astiz MA, Álvarez JA, Gutiérrez-Solana F. Modelo numérico para analizar el efecto del hidrógeno sobre los procesos de fisuración dúctil. *An Mec Fract*. 1998;15:79-84.
60. Tada H, Paris PC, Irwin GR. The stress analysis of cracks handbook. 3rd ed. United States: ASME Press; 2010.
61. Li Y, Gong B, Li X, Deng C, Wang D. Specimen thickness effect on the property of hydrogen embrittlement in single edge notch tension testing of high strength pipeline steel. *Int J Hydrogen Energy*. 2018;43(32):15575-85.
62. Giarola J, Avila J, Cintho O, Pinto H, Oliveira M, Bose WW Fo. The effect of hydrogen on the fracture toughness of friction-stir welded API 5L X70 pipeline steels. *Fatigue Fract Eng Mater Struct*. 2022;45(10):3009-24.
63. Xing Y, Yang Z, Yao X, Wang X, Lu M, Zang L, et al. Effects of hydrogen on the fracture toughness of X80 steel base metal and girth weld under strong cathodic current with in situ hydrogen charging. *Eng Fail Anal*. 2022;135:106143-57.
64. Chatzidouros E, Traidia A, Devarapalli R, Pantelis D, Steriotis T, Jouiad M. Effect of hydrogen on fracture toughness properties of a pipeline steel under simulated sour service conditions. *Int J Hydrogen Energy*. 2018;43(11):5747-59.
65. Tosun U. Investigating the Fracture Behaviour of X70M linepipe steel girth weldments via single edge notched tension and bend tests [dissertation]. Turkey: Middle East Technical University; 2018.
66. Moore P, Pisarski H. SENT testing standard BS 8571 and its ongoing development. *Int J Press Vessels Piping*. 2017;156:2-7.
67. Shen G, Gianetto J, Tyson W. Measurement of J-R Curves using single specimen technique on clamped SE(T) specimens. In: Nineteenth International Offshore and Polar Engineering Conference; 2009

- Jul 21-26; Osaka, Japan. Proceedings. Cupertino, United States: International Society of Offshore and Polar Engineers; 2009.
68. Cravero S, Ruggieri C. Estimation procedure of J-resistance curves for SE(T) fracture specimens using unloading compliance. *Eng Fract Mech.* 2007;74(17):2735-57.
  69. Ruggieri C. Further results in J and CTOD estimation procedures for SE(T) fracture specimens—Part I: homogeneous materials. *Eng Fract Mech.* 2012;79:245-65.
  70. Neeraj T, Srinivasan R, Li J. Hydrogen embrittlement of ferritic steels: observations on deformation microstructure, nanoscale dimples and failure by nanovoiding. *Acta Mater.* 2012;60(13-14):5160-71.
  71. Haag J. Influência da geometria do corpo de prova e do tamanho de trinca na tenacidade à fratura do aço API 5DP tool joint [dissertation]. Porto Alegre: Universidade Federal do Rio Grande do Sul; 2015.
  72. Djukic MB, Bakic GM, Zeravcic VS, Sedmak A, Rajicic B. The synergistic action and interplay of hydrogen embrittlement mechanisms in steels and iron: localized plasticity and decohesion. *Eng Fract Mech.* 2019;216:106528-60.